Uncovering the Triplet Ground State of Triangular Graphene Nanoflakes Engineered with Atomic Precision on a Metal Surface

Jingcheng Li[ ],[1] Sofia Sanz[ ],[2] Jesus Castro-Esteban,[3] Manuel Vilas-Varela,[3] Niklas Friedrich[ ],[1] Thomas Frederiksen[ ],[2,4,*] Diego Peña,[3,†] and Jose Ignacio Pascual[ ][1,4,‡]

[1]*CIC Nanogune BRTA, 20018 Donostia-San Sebastián, Spain*
[2]*Donostia International Physics Center (DIPC), 20018 Donostia-San Sebastián, Spain*
[3]*Centro Singular de Investigación en Química Biolóxica e Materiais Moleculares (CiQUS), and Departamento de Química Orgánica, Universidade de Santiago de Compostela, 15705 Santiago de Compostela, Spain*
[4]*Ikerbasque, Basque Foundation for Science, 48013 Bilbao, Spain*

Graphene can develop large magnetic moments in custom-crafted open-shell nanostructures such as triangulene, a triangular piece of graphene with zigzag edges. Current methods of engineering graphene nanosystems on surfaces succeeded in producing atomically precise open-shell structures, but demonstration of their net spin remains elusive to date. Here, we fabricate triangulenelike graphene systems and demonstrate that they possess a spin $S = 1$ ground state. Scanning tunneling spectroscopy identifies the fingerprint of an underscreened $S = 1$ Kondo state on these flakes at low temperatures, signaling the dominant ferromagnetic interactions between two spins. Combined with simulations based on the meanfield Hubbard model, we show that this $S = 1$ π paramagnetism is robust and can be turned into an $S = 1/2$ state by additional H atoms attached to the radical sites. Our results demonstrate that π paramagnetism of high-spin graphene flakes can survive on surfaces, opening the door to study the quantum behavior of interacting π spins in graphene systems.

In spite of their apparent simplicity, custom-crafted graphene nanoflakes (GNFs) are predicted to exhibit complex magnetic phenomenology [1] with promising possibilities as active components of a new generation of nanoscale devices [2–4]. As predicted by Lieb's theorem for bipartite lattices [5], certain shapes of graphene structures may accommodate a spin imbalance in the π electron cloud, resulting in GNFs with a net magnetic moment. Graphene π paramagnetism is more delocalized, mobile, and isotropic than conventional magnetism from d or f states [6] and can be electrically addressed [7,8]. Furthermore, the magnetic moments and their correlations in GNFs can be precisely engineered through their sizes, edge topology, or chemical doping [9–12].

The fabrication of such GNFs has been hindered due to their high reactivity [13]. Because they are open-shell structures, the presence of unpaired electrons (radicals) makes the synthesis difficult. Initially, unsubstituted triangulene was synthesized by dehydrogenating precursor molecules with the tip of a scanning tunneling microscope (STM) [14]. Very recently, triangular GNFs with larger sizes have been synthesized through an on-surface synthetic (OSS) approach [15–17], a strategy for fabricating atomically precise graphene flakes on a metallic surface [18–21]. Despite such progress in fabrication, the magnetic properties of triangular GNFs on a surface have not been demonstrated experimentally.

Here we report the OSS fabrication of triangulenelike GNFs and demonstrate that the GNFs have a triplet ground state. The synthesized GNFs have reduced symmetry compared to triangulene, which increases the localization of the magnetic moments. High-resolution STM images and spectroscopy allow us to identify the two spin centers on the GNFs and map their distribution. Their ferromagnetic correlations are characterized by the spin-1 Kondo effect [22–24], which happens due to the incomplete screening of two coupled spins by conducting electrons of the metal substrate. Our results also show that the strength of correlations between spins depends on the distance between them.

Figure 1(a) shows the chemical structures of the GNF characterized in the experiments, named here extended triangulene (ETRI). This GNF has 19 carbon atoms in one sublattice (highlighted by red circles) and 17 carbon atoms in the other (black circles), which results in a total spin $S = 1$ according to Lieb's theorem [5]. For comparison, we also produced the GNF in Fig. 1(b) [named as double triangulene (DTRI)], which has 22 carbon atoms in both sublattices and thus a spin $S = 0$ ground state. We synthesized these GNFs by depositing the respective molecular precursors, shown in Figs. 1(c) and 1(d) [details in Supplemental Material (SM) [25]], on a Au(111) surface at 330 °C. The hot surface activates a simultaneous debromination and cyclodehydrogenation step that planarizes them into their final structures.
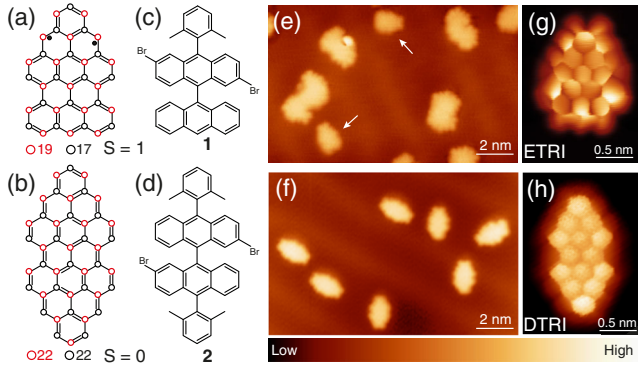
FIG. 1. Chemical structures and synthetic route of extended triangulene and double triangulene. (a), (b) Atomic structures of ETRI and DTRI, which have spin 1 and 0, respectively. Red (black) open circles denote carbon atoms that belong to different sublattices, with the total number of carbon atoms indicated under the structures. (c), (d) Molecular precursors 2,6-dibromo-10-(2,6-dimethylphenyl)-9,9'-bianthracene (precursor 1) and 2,2'-dibromo-10,10'-bis(2,6-dimethylphenyl)-9,9'-bianthracene (precursor 2) used to synthesize ETRI and DTRI, respectively. (e), (f) STM overview images ($V = 0.3$ V, $I = 0.1$ nA) of the formed GNFs from precursors 1 and 2, respectively. The arrows in (e) indicate the ETRI monomers created. (g), (h) Constant height current images ($V = 2$ mV) of ETRI and DTRI with a CO-terminated tip.

Low-temperature STM overview images of the Au (111) surface after deposition of precursors 1 and 2 are shown in Figs. 1(e) and 1(f), respectively. While the reacted precursor 1, ETRI, appears on the surface mostly as monomers and dimers in a ratio of approximately 1 : 7, nearly all deposited precursors 2, DTRI, remain as monomer species. In every case, the monomers adopt a planar configuration, as expected for the structures in Figs. 1(a) and 1(b). Furthermore, high-resolution STM current images using a CO-terminated tip [34,35] [Figs. 1(g) and 1(h)] reproduce the chemical bond structures of Figs. 1(a) and 1(b), indicating the successful synthesis of ETRI and DTRI. It is worth noting that the current image of DTRI shows merely the backbone structure, as also observed in similar symmetric systems [36], while the current image of ETRI shows additional bright features at the edges. Considering that these images were recorded at 2 mV, the bright features surrounding the backbone structure indicate an enhancement of the local density of states (LDOS) close to Fermi level for the ETRI molecule.

The different shape in the images is better manifested in differential conductance (dI/dV) spectra measured on both types of GNFs [Fig. 2(a)]. The spectrum on ETRI shows a pronounced and narrow (FWHM $\sim$ 1 meV) dI/dV peak centered at zero bias. The zero-bias peak broadens anomalously fast with temperature [as described in Fig. 2(b)] and splits with magnetic fields [Fig. 2(c)], demonstrating that it is a manifestation of the Kondo effect [37]. A (zero-bias) Kondo-derived resonance reflects the screening of a local

spin by conduction electrons [38] and, hence, is a direct proof of the presence of localized magnetic moments on ETRI even when it lies on a metal surface. On the contrary, the spectra taken on DTRI are featureless. Furthermore, both wide-bias range spectra and dI/dV maps reveal their closed-shell ground state (see SM [25]).

The temperature and magnetic field dependence of the Kondo resonances provide further insight on the nature of the spin state of ETRI. Although the Kondo effect is frequently described on $S = 1/2$ systems, it also occurs for higher spin configurations [23,24]. For $S = 1$, a zero-bias resonance reflects a partly screened spin, i.e., with only one interaction channel with the substrate [42]. Similar to the spin-1/2 case, the resonance broadens with temperature [with a Kondo temperature $T_K \sim 6$ K, after Fig. 2(b); see SM [25]] but shows a larger sensitivity to the magnetic field [23,24]. While the Kondo resonance of a $S = 1/2$ system in the strong coupling regime ($T < T_K$) splits linearly with magnetic fields only above a critical field $B_c \geq 0.5 k_B T_K / g \mu_b$ [7,43], an underscreened $S = 1$ conserves some magnetic moment, and its zero-bias resonance splits already with $B > 0$ [23,24]. In tunneling spectra, such a peak split should become visible as soon as the Zeeman energy is greater than the thermal broadening ($k_B T$), which, at the 1.2 K of our experimental set up corresponds to fields above 1 Tesla. If the Kondo resonance in Fig. 2(b) were caused by an $S = 1/2$ state, it should appear split in the spectra only for magnetic fields above 3.5 T. However, the peak appears split already at $B = 1.5$ T, proving that the ETRI molecule has an $S = 1$ in an underscreened Kondo state on the gold substrate [25].

The $S = 1$ configuration of the triangular GNFs was further supported by tip-induced manipulation experiments. Because of their biradical character, the zigzag sites show some reactivity and are frequently found passivated by hydrogen atoms produced during the OSS reactions [7,44]. The passivated carbon sites can be identified in high-resolution images by their larger bond length [45] due to the change from sp^2 to sp^3 hybridization. The STM image in Fig. 3(a) shows the bare backbone structure of an ETRI molecule with its characteristic bright features missing due to two additional H atoms passivating the zigzag sites , with its chemical structure shown in Fig. 3(b). The corresponding dI/dV spectrum is featureless around zero bias [black curve in Fig. 3(g)], explaining the absence of bright features in the STM image.

We first cut off one of the passivated H atoms by placing the STM tip on top of site no. 1 in Fig. 3(a) and ramping up the sample bias above 1.5 V [7,44]. The H removal was monitored by a sudden step in the tunneling current [7]. The STM image afterwards appeared with an enhanced LDOS signal around the no. 1 site [Fig. 3(c)], and the dI/dV spectrum on site no. 1 presented a pronounced zero-energy peak [red Fig. 3(g)]. We identify this as $S = 1/2$
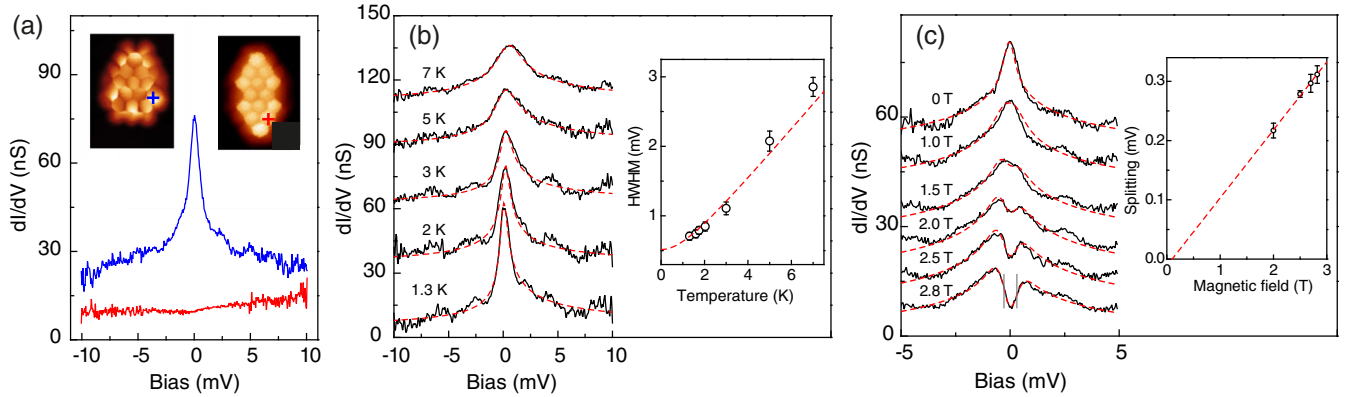
FIG. 2. Kondo resonances in extended triangulene. (a) dI/dV spectra of ETRI (blue curve) and DTRI (red curve) measured at the sites indicated by the colored crosses in the inset. (b) Temperature dependence of the Kondo resonance for an ETRI molecule. The inset plots the half width at half maximum (HWHM) at each temperature, extracted by fitting a Frota function (red dashed lines) [39] and corrected for the thermal broadening of the tip [40]. The plot includes the empirical expression $\sqrt{(\alpha k_B T)^2 + (2k_B T_K)^2}$ [41], fitting the results with $T_K \sim 6$ K and $\alpha = 8.5$. The temperature evolution of the zero-bias conductance, shown as SM [25], agrees with a spin-polarized state in the Kondo regime with energy scale of a few Kelvin. (c) Magnetic field dependence of the Kondo resonance with the field strength indicated in the figure, measured at $T = 1.3$ K. The red dashed lines show the simulated curves using a model for a spin-1 system using the code of Ref. [38]. The inset shows the dependence of Zeeman splitting of the Kondo resonance with magnetic fields, determined from the bias position of steepest slope (indicated on the spectrum at 2.8 T). The dashed line fits the Zeeman splitting with a g factor of 1.98 ± 0.07. The spectra in (b), (c) are shifted vertically for clarity.

Kondo resonance [7] resulting from the single radical state recovered by the removal of the extra H atom at site no. 1 [Fig. 3(d)]. Following a similar process to cleave the second H-CH bond at site no. 2 recovered bright current features all around the ETRI backbone, resembling the shape of the reference biradical structure of Fig. 1(g). The spectrum

measured again over site no. 1 now shows the Kondo resonance with smaller amplitude and linewidth similar to the one in Fig. 2(a), agreeing with its underscreened $S = 1$ state. As quantified in Fig. 3(h), the Kondo resonance of the doubly dehydrogenated GNFs appeared repetitively with a linewidth of about HWHM~0.7 meV, significantly smaller
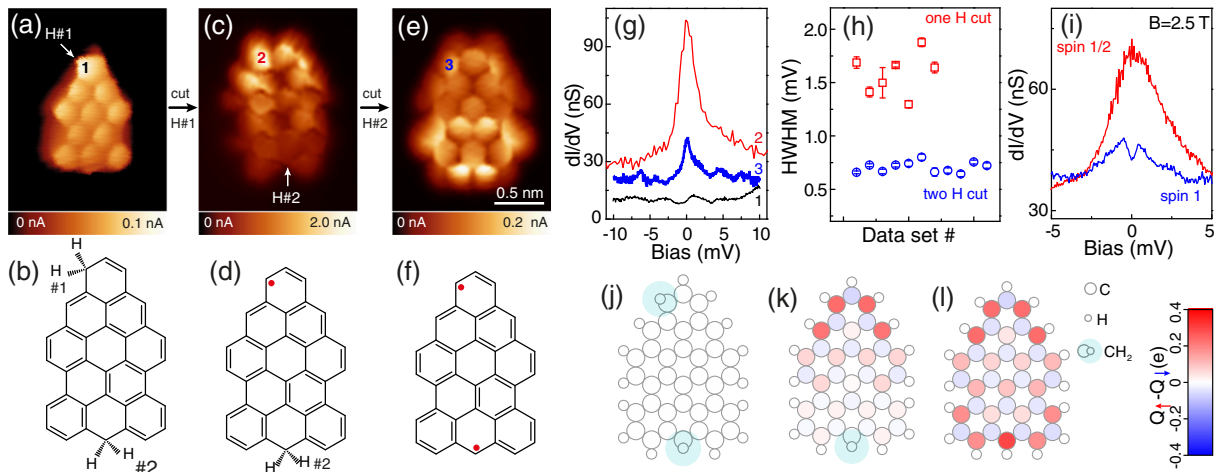

FIG. 3. Spin manipulation by electron-induced removal of extra H atoms. (a) Constant height current image ($V = 2$ mV) of a 2H-ETRI, with its chemical structure shown in (b). (c), (e) Constant height current image ($V = 2$ mV) of the same ETRI of (a) after the electron-induced removal of one and two passivating hydrogen atoms, respectively. The arrows in (a), (c) indicate the STM tip positions during the processes. The corresponding chemical structures are show in (d), (f). (g) Comparison of dI/dV spectra taken on the three structures at the locations noted with numbers in (a), (c), (e). (h) Comparison of the HWHM from the Kondo resonance taken on 1H-ETRI (red data points) and ETRI (blue data points), respectively. The value of each data point is extracted by fitting the corresponding Kondo resonances with Frota functions [39]. Different data points stand for the measurements from different molecules. (i) Comparison of Kondo resonance taken on 1H-passivated ETRI (red curve) and ETRI (blue curve) at a magnetic field of 2.5 T. (j), (k), (l) Spin polarization of 2H-ETRI, 1H-ETRI, and ETRI from meanfield Hubbard simulations.

than in the singly passivated species hinting at their different Kondo states. The spin assignment of each species was further corroborated by comparing their response to a magnetic field of 2.5 T. While the intermediate $S = 1/2$ specie did not present any detectable split of the Kondo resonance, the biradical one exhibited a clear split, as in Fig. 2(c), demonstrating the larger spin polarization of its $S = 1$ underscreened ground state.

The emergence of magnetism in ETRI is reproduced by both meanfield Hubbard (MFH) and density functional theory (DFT) simulations (see SM [25]). Similar to the case of triangulene [1,46], this modified GNF presents two (singly occupied) zero-energy modes, with a triplet ground state clearly preferred over a singlet one by more than 60 meV (see Figs. S9 and S16). The spin polarization [Fig. 3(l)] shows two spin centers localized at opposite sides of the triangular GNF, with a distribution that resembles the experimental current maps [Figs. 1(g) and 3(e)]. We note that their ferromagnetic exchange inter-action is much larger than the Kondo energy scale ($k_B T_K < 1$ meV), thus explaining the $S = 1$ underscreened Kondo ground state found in the experiments. MFH simulations also show that hydrogen passivation of the radical states quenches the spins sequentially, turning ETRI into an $S = 1/2$ doublet [Fig. 3(k)] or completely non-magnetic [Fig. 3(j)], as demonstrated by the electron-induced removal of extra H atoms in the experiments.

A paramagnetic ground state was also found on molecular dimers formed during the OSS process [as shown in Fig. 1(e)], but their larger size crucially affects their magnetic properties. Fig. 4(a) shows a high-resolution image of a dimer. Two ETRI moieties are covalently linked together [Fig. 4(b)] following the Ullmann-like C-C coupling of their halogenated sites [47]. During the cyclo-dehydrogenation step, an extra pentagonal ring is created between them, as highlighted by a red bond in Fig. 4(b), reducing the number of radicals of the dimer to only two. The biradical state is experimentally demonstrated in the SM [25].

The STM image of Fig. 4(a) also reproduces bright features around the dimer backbone (indicated with dashed ellipses) corresponding to the localization of the Kondo effect: dI/dV spectra measured on either of the two show pronounced peaks centered at zero bias [Fig. 4(c)], which broaden with temperature [Fig. 4(d)] and magnetic field [Fig. 4(e)]. However, these Kondo resonances broaden faster with T than for the $S = 1$ case of ETRI [both compared in the inset of Fig. 4(d)] and show no split at $B = 2.7$ T, signaling a different magnetic ground state.

Our MFH simulations of ETRI dimers like in Fig. 4(b) confirm their biradical state, but the energy between triplet and singlet solutions are now closer (see SM). On a surface, a magnetic ground state probably behaves as two noninteracting $S = 1/2$ spins. This explains the lack of B-induced split and the faster broadening with T expected
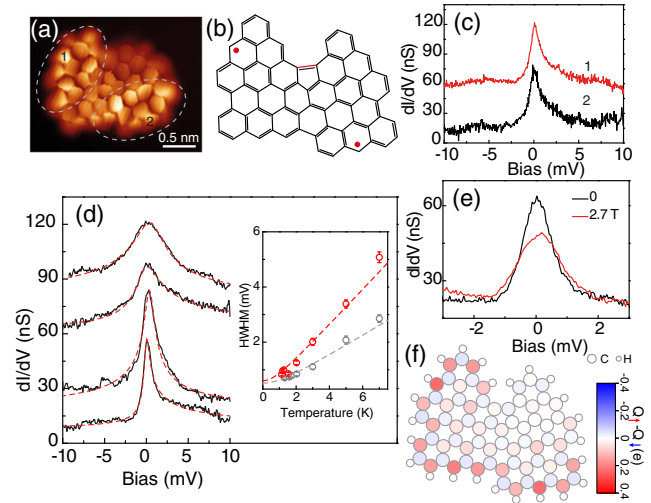

FIG. 4. Magnetic properties of dimers of ETRI. (a) Constant height current image ($V = 2$ mV) of a ETRI dimer with its chemical structure shown in (b). (c) dI/dV spectra taken on the dimer on the sites indicated with corresponding numbers in (a). (d) Temperature dependence of the Kondo resonance taken at site no.2. The spectra are shifted vertically for clarity. The inset plots the HWHM at each temperature, extracted by fitting a Frota function (red dashed lines) [39] and corrected for the thermal broadening of the tip [40]. The inset includes the simulation with the empirical expression $\sqrt{(\alpha k_B T)^2 + (2k_B T_K)^2}$ [41], fitting the results with $T_K \sim 7$ K with $\alpha = 15$. For comparison, the temperature dependence of HWHM from the Kondo resonance taken on a single ETRI monomer (gray data points) is also shown. (e) Kondo resonance taken at location 2 at different magnetic fields at $T = 1.3$ K. (f) Spin polarization of a ETRI dimer from MFH simulations.

for $S = 1/2$ Kondo systems [24]. The spin polarization maps obtained from MFH simulations reproduce the bright current regions on the dimers well [Fig. 4(f)], further corroborating that this signal can be associated to the spin distribution. The origin of such a small magnetic exchange between the two radical states is related to the presence of a pentagon between them and to the larger separation between the two spin centers. In fact, in the absence of this extra C-C bond, MFH simulations find a robust $S = 2$ ground state. Thus, pentagonal rings embedded in certain sites of an open-shell GNF can affect its magnetic state critically by quenching a radical state and modifying the total spin (here by $\Delta S = 1$) [48], just as extra hydrogen atoms do [7], but their placement on a specific site can be designed precisely during the OSS process.

In summary, we have demonstrated the magnetic ground state of graphene flakes fabricated deterministically with a triangularlike shape. The survival of the $S = 1$ state on the metal surface is identified first through the observation of a narrow Kondo resonance, that reacts to magnetic fields as an underscreened spin triplet. The $S = 1$ state was further confirmed through removal of hydrogen atoms by tip

manipulation experiments, which revealed the stepwise emergence of two spins localized at different sides of the flakes. We note that our findings here contrast with the absence of magnetic signals in previous studies of larger triangulene flakes [15,16]. It is therefore an interesting subject for future work to unveil the precise interplay between size and symmetry of GNFs for their magnetic state over a metal surface. Nevertheless, the existence of GNFs with a net spin on a surface opens the door to new investigations of their spin dynamics and coherence over inorganic supports, which are crucial aspects for utilizing graphene nanosystems [49] in quantum spintronic applications.

---

[*]thomas_frederiksen@ehu.eus

[†]diego.pena@usc.es

[‡]ji.pascual@nanogune.eu

[1] O. V. Yazyev, Rep. Prog. Phys. **73**, 056501 (2010).

[2] W. L. Wang, O. V. Yazyev, S. Meng, and E. Kaxiras, Phys. Rev. Lett. **102**, 157201 (2009).

[3] W. Han, R. K. Kawakami, M. Gmitra, and J. Fabian, Nat. Nanotechnol. **9**, 794 (2014).

[4] Z. Bullard, E. C. Girão, J. R. Owens, W. A. Shelton, and V. Meunier, Sci. Rep. **5**, 7634 (2015).

[5] E. H. Lieb, Phys. Rev. Lett. **62**, 1201 (1989).

[6] B. Trauzettel, D. V. Bulaev, D. Loss, and G. Burkard, Nat. Phys. **3**, 192 (2007).

[7] J. Li, S. Sanz, M. Corso, D. J. Choi, D. Peña, T. Frederiksen, and J. I. Pascual, Nat. Commun. **10**, 200 (2019).

[8] S. Mishra, D. Beyer, K. Eimre, S. Kezilebieke, R. Berger, O. Gröning, C. A. Pignedoli, K. Müllen, P. Liljeroth, P. Ruffieux, X. Feng, and R. Fasel, Nat. Nanotechnol. **15**, 22 (2020).

[9] J. Fernández-Rossier and J. J. Palacios, Phys. Rev. Lett. **99**, 177204 (2007).

[10] W. L. Wang, S. Meng, and E. Kaxiras, Nano Lett. **8**, 241 (2008).

[11] E. Kan, W. Hu, C. Xiao, R. Lu, K. Deng, J. Yang, and H. Su, J. Am. Chem. Soc. **134**, 5718 (2012).

[12] M. E. Sandoval-Salinas, A. Carreras, and D. Casanova, Phys. Chem. Chem. Phys. **21**, 9069 (2019).

[13] E. Clar and D. G. Stewart, J. Am. Chem. Soc. **75**, 2667 (1953).

[14] N. Pavliček, A. Mistry, Z. Majzik, N. Moll, G. Meyer, D. J. Fox, and L. Gross, Nat. Nanotechnol. **12**, 308 (2017).

[15] S. Mishra, D. Beyer, K. Eimre, J. Liu, R. Berger, O. Gröning, C. A. Pignedoli, K. Müllen, R. Fasel, X. Feng, and P. Ruffieux, J. Am. Chem. Soc. **141**, 10621 (2019).

[16] J. Su, M. Telychko, P. Hu, G. Macam, P. Mutombo, H. Zhang, Y. Bao, F. Cheng, Z.-Q. Huang, Z. Qiu, S. J. R. Tan, H. Lin, P. Jelínek, F.-C. Chuang, J. Wu, and J. Lu, Sci. Adv. **5**, eaav7717 (2019).

[17] S. Mishra, D. Beyer, K. Eimre, R. Ortiz, J. Fernandez-Rossier, R. Berger, O. Gröning, C. A. Pignedoli, R. Fasel, X. Feng, and P. Ruffieux, arXiv:2003.00753.

[18] J. Cai, P. Ruffieux, R. Jaafar, M. Bieri, T. Braun, S. Blankenburg, M. Muoth, A. P. Seitsonen, M. Saleh, X. Feng, K. Mullen, and R. Fasel, Nature (London) **466**, 470 (2010).

[19] M. Treier, C. A. Pignedoli, T. Laino, R. Rieger, K. Müllen, D. Passerone, and R. Fasel, Nat. Chem. **3**, 61 (2011).

[20] P. Ruffieux, S. Wang, B. Yang, C. Sánchez-Sánchez, J. Liu, T. Dienel, L. Talirz, P. Shinde, C. A. Pignedoli, D. Passerone, T. Dumslaff, X. Feng, K. Müllen, and R. Fasel, Nature (London) **531**, 489 (2016).

[21] S. Clair and D. G. de Oteyza, Chem. Rev. **119**, 4717 (2019).

[22] S. Sasaki, S. De Franceschi, J. M. Elzerman, W. G. van der Wiel, M. Eto, S. Tarucha, and L. P. Kouwenhoven, Nature (London) **405**, 764 (2000).

[23] N. Roch, S. Florens, T. A. Costi, W. Wernsdorfer, and F. Balestro, Phys. Rev. Lett. **103**, 197202 (2009).

[24] J. J. Parks, A. R. Champagne, T. A. Costi, W. W. Shum, A. N. Pasupathy, E. Neuscamman, S. Flores-Torres, P. S. Cornaglia, A. A. Aligia, C. A. Balseiro, G. K. L. Chan, H. D. Abruña, and D. C. Ralph, Science **328**, 1370 (2010).

[25] See Supplemental Material at http://link.aps.org/supplemental/10.1103/PhysRevLett.124.177201 for synthesis and methods details, and for complementary experimental results and simulations, which includes Refs. [24–31].

[26] Y. Hancock, A. Uppstu, K. Saloriutta, A. Harju, and M. J. Puska, Phys. Rev. B **81**, 245402 (2010).

[27] N. Papior, sisl: v0.9.6 (2019).

[28] Y. Hirshberg and E. Fischer, J. Chem. Soc. 629 (1953).

[29] D. Goldhaber-Gordon, J. Göres, M. A. Kastner, H. Shtrikman, D. Mahalu, and U. Meirav, Phys. Rev. Lett. **81**, 5225 (1998).

[30] D. P. Daroca, P. Roura-Bas, and A. A. Aligia, Phys. Rev. B **98**, 245406 (2018).

[31] R. Ortiz, N. A. García-Martínez, J. L. Lado, and J. Fernández-Rossier, Phys. Rev. B **97**, 195425 (2018).

[32] J. M. Soler, E. Artacho, J. D. Gale, A. García, J. Junquera, P. Ordejón, and D. Sánchez-Portal, J. Phys. Condens. Matter **14**, 2745 (2002).

[33] J. P. Perdew, K. Burke, and M. Ernzerhof, Phys. Rev. Lett. **77**, 3865 (1996).

[34] L. Gross, F. Mohn, N. Moll, P. Liljeroth, and G. Meyer, Science **325**, 1110 (2009).

[35] G. Kichin, C. Weiss, C. Wagner, F. S. Tautz, and R. Temirov, J. Am. Chem. Soc. **133**, 16847 (2011).

[36] D. Beyer, S. Wang, C. A. Pignedoli, J. Melidonie, B. Yuan, C. Li, J. Wilhelm, P. Ruffieux, R. Berger, K. Müllen, R. Fasel, and X. Feng, J. Am. Chem. Soc. **141**, 2843 (2019).

[37] M. Ternes, A. J. Heinrich, and W.-D. Schneider, J. Phys. Condens. Matter **21**, 053001 (2009).

[38] M. Ternes, New J. Phys. **17**, 063016 (2015).

[39] H. O. Frota, Phys. Rev. B **45**, 1096 (1992).

[40] Y.-H. Zhang, S. Kahle, T. Herden, C. Stroh, M. Mayor, U. Schlickum, M. Ternes, P. Wahl, and K. Kern, Nat. Commun. **4**, 2110 (2013).

[41] K. Nagaoka, T. Jamneala, M. Grobis, and M. F. Crommie, Phys. Rev. Lett. **88**, 077205 (2002).

[42] M. Pustilnik and L. I. Glazman, Phys. Rev. Lett. **87**, 216601 (2001).

[43] T. A. Costi, Phys. Rev. Lett. **85**, 1504 (2000).

[44] L. Talirz, H. Söde, J. Cai, P. Ruffieux, S. Blankenburg, R. Jafaar, R. Berger, X. Feng, K. Müllen, D. Passerone, R. Fasel, and C. A. Pignedoli, J. Am. Chem. Soc. **135**, 2060 (2013).

[45] L. Gross, F. Mohn, N. Moll, B. Schuler, A. Criado, E. Guitián, D. Peña, A. Gourdon, and G. Meyer, Science **337**, 1326 (2012).

[46] R. Ortiz, R. Á. Boto, N. García-Martínez, J. C. Sancho-García, M. Melle-Franco, and J. Fernández-Rossier, Nano Lett. **19**, 5991 (2019).

[47] D. G. De Oteyza, A. García-Lekue, M. Vilas-Varela, N. Merino-Díez, E. Carbonell-Sanromà, M. Corso, G. Vasseur, C. Rogero, E. Guitián, J. I. Pascual, J. E. Ortega, Y. Wakayama, and D. Peña, ACS Nano **10**, 9000 (2016).

[48] S. Mishra, D. Beyer, R. Berger, J. Liu, O. Gröning, J. I. Urgel, K. Müllen, P. Ruffieux, X. Feng, and R. Fasel, J. Am. Chem. Soc. **142**, 1147 (2020).

[49] F. Lombardi, A. Lodi, J. Ma, J. Liu, M. Slota, A. Narita, W. K. Myers, K. Müllen, X. Feng, and L. Bogani, Science **366**, 1107 (2019).

Uncovering the triplet ground state of triangular graphene nanoflakes engineered with atomic precision on a metal surface

Jingcheng Li,[1] Sofia Sanz,[2] Jesus Castro-Esteban,[3] Manuel Vilas-Varela,[3] Niklas Friedrich,[1] Thomas Frederiksen,[2,4,*] Diego Peña,[3,†] and Jose Ignacio Pascual[1,4,‡]

[1]*CIC nanoGUNE, 20018 Donostia-San Sebastián, Spain*
[2]*Donostia International Physics Center (DIPC), 20018 Donostia-San Sebastián, Spain*
[3]*Centro Singular de Investigación en Química Biolóxica e Materiais*
Moleculares (CiQUS), and Departamento de Química Orgánica,
Universidade de Santiago de Compostela, 15782 Santiago de Compostela, Spain
[4]*Ikerbasque, Basque Foundation for Science, 48013 Bilbao, Spain*

Contents

METHODS

Sample preparation and measurement details.

The experiments were performed on two different scanning tunneling microscopes (STM) operating in ultra-high vacuum, a commercial JT STM (from specs) operated at 1.2 K with a magnetic field up to 3 Tesla and a home made STM operating at 5 K. Both setups allow in situ sample preparation and transfer into the STM. The Au(111) substrate was cleaned in UHV by repeated cycles of Ne^+ ion sputtering and subsequent annealing to 730 K. The molecular precursors were sublimated from a Knudsen cell onto the clean Au(111) substrate kept at 330 °C separately. The evaporation temperatures of molecular precursor **1,2** are 230 °C and 210 °C, respectively. Then the two samples were characterized separately. A tungsten tip functionalized with a CO molecule was used for high resolution images. The high resolution images in the manuscript were acquired in constant height mode, at very small voltages, and junction resistances of typically 20 MΩ. The dI/dV signal was recorded using a lock-in amplifier at 760 Hz. The bias modulation is $V_{rms} = 0.1$ mV for short range spectra ($\pm$ 10 mV), and $V_{rms} = 4$ mV for wide range spectra ($\pm$ 1 V). The Kondo state presented in the manuscript was reproducibly observed in all the species inspected that had no hydrogen passivation (more than 25). In two of them, the temperature-dependence was measured with similar results.

Simulations with the meanfield Hubbard model.

In order to understand the experimental observations, we performed simulations based on the meanfield Hubbard (MFH) model, which provides a good description for carbon π-electron systems [1]. Comparison with more accurate density functional theory (DFT) calculations is provided in Sec. . We described the sp^2 carbon backbone of the different molecules with the following Hamiltonian: $H = \sum_{ij\sigma} t_{ij}(c_{i\sigma}^{\dagger}c_{j\sigma} + \text{h.c.}) + U\sum_i \left(n_{i\uparrow}\langle n_{i\downarrow}\rangle + \langle n_{i\uparrow}\rangle n_{i\downarrow} - \langle n_{i\uparrow}\rangle\langle n_{i\downarrow}\rangle\right)$ where $c_{i\sigma}^{\dagger}$ is the creation operator and $n_{i\sigma} = c_{i\sigma}^{\dagger}c_{i\sigma}$ the corresponding density operator of electrons with spin σ in the p_z orbital centered at atomic site i. We consider tight-binding hopping amplitudes in an orthogonal basis, $t_1 = 2.7$ eV, $t_2 = 0.2$ eV, and $t_3 = 0.18$ eV for first, second, and third-nearest neighbor matrix elements (defined from interatomic distances $d_1 < 1.6\text{Å} < d_2 < 2.6\text{Å} < d_3 < 3.1\text{Å}$) that originate from Refs. [1, 2]. The on-site Coulomb repulsion $U = 3$ eV was taken as an empirical parameter, providing a good agreement with DFT for nanographenes [1], see also Sec. . The self-consistent solution of the MFH Hamiltonian is computed with a custom-made implementation based on SISL [3]. The local spin density is obtained from the difference $\langle n_{i\uparrow} - n_{i\downarrow}\rangle$.

SYNTHESIS OF MOLECULAR PRECURSORS 1 AND 2

General methods for the synthesis of the precursors.

All reactions were carried out under argon using oven-dried glassware. TLC was performed on Merck silica gel 60 F254; chromatograms were visualized with UV light (254 and 360 nm). Flash column chromatography was performed on Merck silica gel 60 (ASTM 230-400 mesh). 1H and 13C NMR spectra were recorded at 300 and 75 MHz or 500 and 125 MHz (Varian Mercury 300 or Bruker DPX-500 instruments), respectively. APCI spectra were determined on a Bruker Microtof instrument. The synthesis of dibromoanthrone 3 (Fig. S1) and dibromobianthrone 5 (Fig. S2) has been previously described [4, 5]. n-BuLi was used in solution in hexane (2.4 M). Commercial reagents were purchased from ABCR, GmbH, Aldrich Chemical Co., or Strem Chemicals Inc., and were used without further purification. Et2O was purified by a MBraun SPS -800 Solvent Purification System.

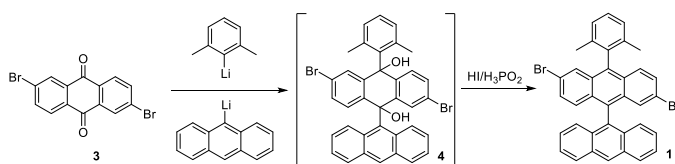**Experimental details for the synthesis of precursor 1.**

FIG. S1: Synthetic route of precursor **1**.

A solution of 2-iodo-1,3-dimethylbenzene (126.1 mg, 0.543 mmol) and 9-bromoanthracene (139.7 mg,0.543 mmol) in Et$_2$O (5 mL) was cooled to 0C. n-BuLi (452 μL, 2.4 M, 1.08 mmol) was added dropwise and the reaction mixture was stirred under argon for 1 h. The reaction was warmed up slowly until room temperature, a solution of compound 3 (100.0 mg, 0.272 mmol) in Et$_2$O (20mL) was added and the mixture was stirred overnight. The reaction was quenched with 1 mL of AcOH and Et$_2$O was removed under reduced pressure. The residue was dissolved in 5 mL of AcOH, and then HI (400 μL, 3.00 mmol, 57%) and H$_3$PO$_2$ (2.0 mL, 22.5 mmol, 50%) were added. The reaction mixture was stirred for 2 h at 80 C. After cooling to room temperature, saturated aqueous solution of NaHCO$_3$ was added and the aqueous phase was extracted with CH$_2$Cl$_2$. The combined organic phases were dried over anhydrous Na$_2$SO$_4$ and the solvent was evaporated under reduced pressure. The resulting mixture was purified by column chromatography (SiO$_2$, CH$_2$Cl$_2$/hexane, 1:4) to afford 2,6-dibromo-10-(2,6-dimethylphenyl)-9,9-bianthracene (1, 23 mg, 14%) as an orange solid. ^{1}CH NMR (300 MHz, CDCl$_3$) : 8.74 (s, 1H), 8.19 (d, J = 8.5 Hz, 2H), 7.72 (d, J =2.0 Hz, 1H), 7.54 7.44 (m, 3H), 7.43 (s, 1H), 7.36 (m, 3H), 7.30 7.27 (m, 1H), 7.25 7.21 (m, 2H), 7.16 (dd, J = 9.2, 2.0 Hz, 1H), 7.06 (d, J = 8.8 Hz, 2H), 6.95 (d, J = 9.3 Hz, 1H), 1.94 (s, 6H) ppm. ^{13}CC NMR (75 MHz, CDCl$_3$) : 137.89 (2xC), 136.66 (C), 136.53 (C), 133.02 (C), 132.73 (C), 131.82 (2xC), 131.80 (2xC), 131.73 (C), 130.77 (C), 130.61 (C), 130.14 (3xCH), 129.37 (CH), 129.10 (CH), 129.02 (2xCH), 128.61 (CH), 128.40 (CH), 128.21 (CH), 128.15 (2xCH), 126.62 (2xCH), 126.54 (2xCH), 125.73 (2xCH), 125.59 (C), 121.18 (C), 121.11 (C), 20.34 (2xCH$_3$) ppm. MS (APCI (M+1)) for C$_{36}$H$_{25}$Br$_2$, found: 615.0318.

Experimental details for the synthesis of precursor 2.
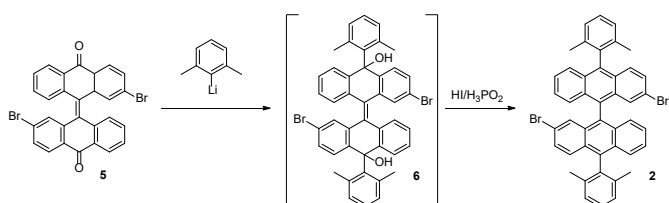

FIG. S2: Synthetic route of precursor **2**.

A solution of (2,6-dimethylphenyl)lithium (5.0 mL, 0.19 M in Et$_2$O, 0.93 mmol) was added dropwise to a suspension of compound 5 (50 mg, 0.093 mmol) in Et$_2$O (15 mL) and the reaction mixture was stirred at room temperature under argon for 20 h. The reaction was quenched with 1 mL of AcOH and Et$_2$O was removed under reduced pressure. The residue was dissolved in 10 mL of AcOH, and then HI (500 μL, 3.80 mmol, 57%) and H$_3$PO$_2$ (1.0 mL, 9.1 mmol, 50%) were added. The reaction mixture was stirred for 2 h at 80 C. After cooling to room temperature, saturated aqueous solution of NaHCO$_3$ was added and the aqueous phase was extracted with CH$_2$Cl$_2$. The combined organic phases were dried over anhydrous Na$_2$SO$_4$ and the solvent was evaporated under reduced pressure. The resulting mixture was purified by column chromatography (SiO$_2$, CH$_2$Cl$_2$/hexane, 1:4) to afford compound 2 (53 mg, 79%) as a violet solid (mp: 180 C). ^{1}H NMR (300 MHz, CDCl$_3$) : 7.62 (d, J = 8.7 Hz, 2H), 7.52 (d, J = 9.2 Hz, 2H), 7.47 (d, J = 7.0 Hz, 2H), 7.42 (d, J = 7.8 Hz, 2H), 7.40 7.33 (m, 6H), 7.30 (d, J = 1.9 Hz, 2H), 7.27 7.15 (m, 2H), 7.12 (d, J = 8.8 Hz, 2H), 1.97 (s, 6H), 1.96 (s, 6H) ppm. ^{13}C NMR (75 MHz, CDCl$_3$) : 137.8 (2C), 137.6 (2C), 137.4 (2C), 137.1 (2C), 132.4 (2C), 132.1 (2C), 131.4 (2C), 129.7 (2C), 129.3 (2CH), 128.6 (2CH), 128.3 (2CH), 128.1 (2CH), 127.8 (2CH), 127.6 (2CH), 127.0 (2CH), 126.7 (2CH), 126.4 (2CH), 126.1 (2CH), 120.8 (2C), 20.3 (2CH$_3$) ppm. MS (EI) m/z (%): 718 (M+, 47), 360 (5). HRMS (EI) for C$_{44}$H$_{32}$Br$_2$: calculated: 718.0871; found: 718.0874.

^{1}H and ^{13}C NMR spectra of precursor 1,2
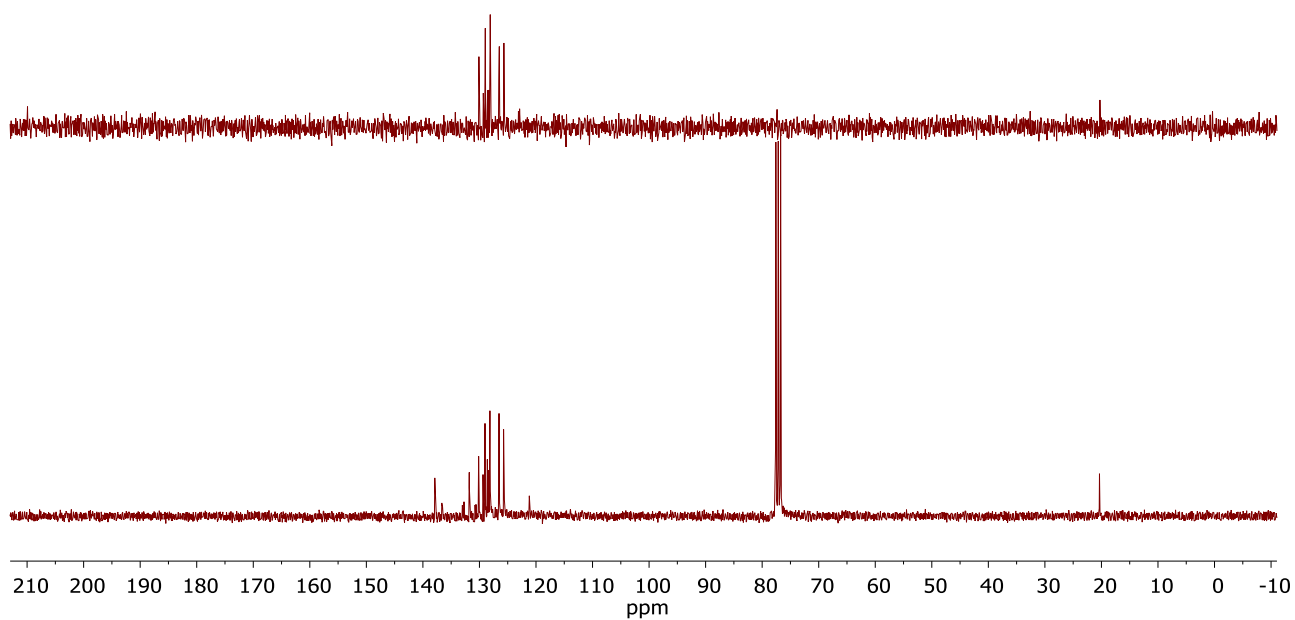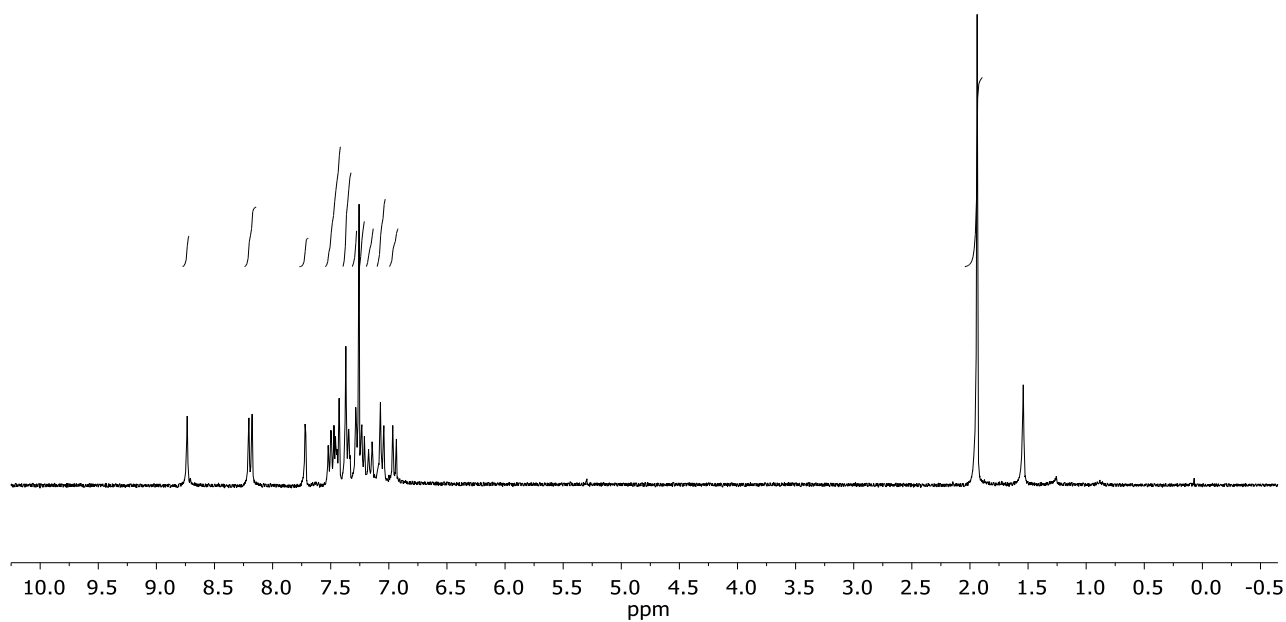
FIG. S3: ^{1}H and ^{13}C NMR spectra of precursor **1**.
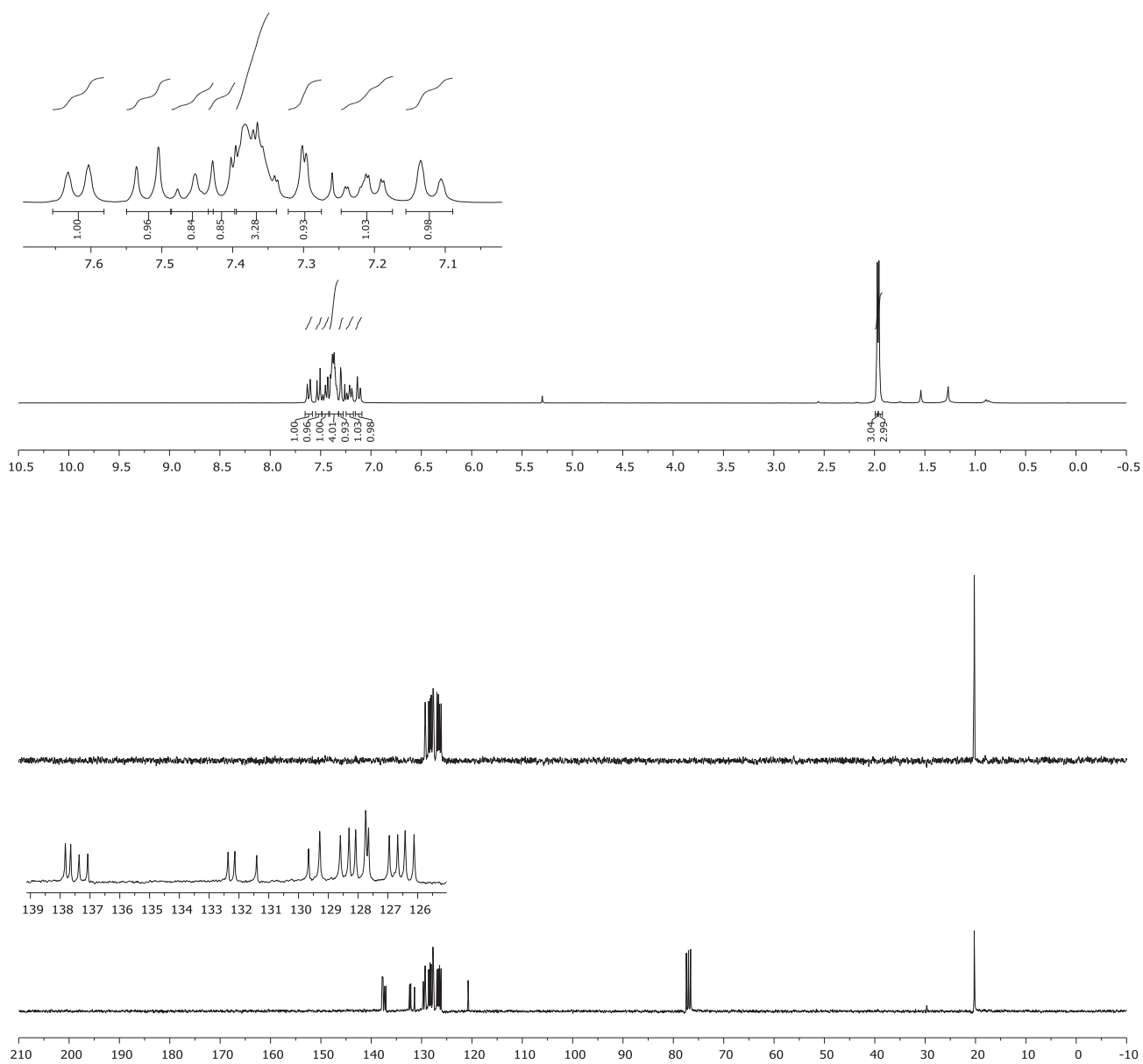
FIG. S4: ^{1}H and ^{13}C NMR spectra of precursor **2**.

TEMPERATURE DEPENDENCE OF THE ZERO-BIAS CONDUCTANCE

The zero-bias conductance (equilibrium conductance) decreases with temperature following an universal form that depends on the spin. For spin 1/2, a phenomenological expression describing this behaviour was provided by Goldhaber Gordon in ref. [6]. In ref. [7], supplementary material, this expression was further scaled to account for higher spin states. The resulting expression for the temperature dependence of the zero-bias conductance of a spin S was:

$$G_S(T) = G(0)[(1 - \Delta_S)g_S(T/T_K) + \Delta_S/2] \tag{1}$$

with

$$g_S(T/T_K) = [1 + (T/T_K')^{\xi_S}]^{-\alpha_S} \tag{2}$$

and

$$T_K' = T_K/(2^{1/\alpha_s} - 1)^{1/\xi_S} \tag{3}$$

In ref. [7] these expressions were used to fit the results from Numerical Renomalization Group simulations of various spin systems S and to obtain phenomenological parameters $\Delta_S, \xi_S, \alpha_S$ for different spin states.

Here, we used eqs. 1-3 to fit the temperature dependence of the amplitude of zero-bias anomalies in ETRI, obtained for the set of spectra with HWHM values shown in Fig. 2b of the manuscript. To properly obtain the resonance's amplitude, it is crucial to account for the thermal broadening of the STM's tip density of states. Therefore, we fitted the spectral zero-bias peaks with a convolution of a Frota function times the derivative of the Fermi Dirac distribution at the corresponding temperature.

The results are shown as points in Fig. S5, including the fit of their evolution with temperature using the phenomenological expression from above with $\alpha_{1/2}$=0.22 and α_1=0.5, and other parameters indicated in Ref. [7] for $S = 1/2$ and $S = 1$ (underscreened), and only T_K and $G(0)$ as fitting parameters. While the HWHM was reasonably extracted for all spectra at the same temperature, the value $G(V = 0, T)$ show more dispersion. We note that the zero bias conductance is sensitive to small variations in tip position (both vertically and laterally), while the FWHM is less affected by these. The fit is not conclusive in a specific spin state due to the data dispersion, and could be similarly fitted by either parameters of $S = 1/2$ or $S = 1$. However, for $S = 1/2$ a Kondo temperature of 6 K is obtained, which is a robust approximation [8], and similar to the Kondo scale deduced from the HWHM vs. T measurements of Fig. 2 of the main text. A spin-1/2 Kondo state with Kondo temperature of 6 K is incompatible with the split of its zero-bias resonance with a magnetic field of only 1.5 T at 1.2 K, as we observed in the experiment. Following Ref. [9], a spin 1/2 with $T_K = 6$ K would split only for magnetic fields larger than 2.5 T and be detected at 1.2 K not before reaching 3.5 T, above our experimental access. This corroborates that a $S = 1$ is the only possible magnetic state compatible with our experiments.
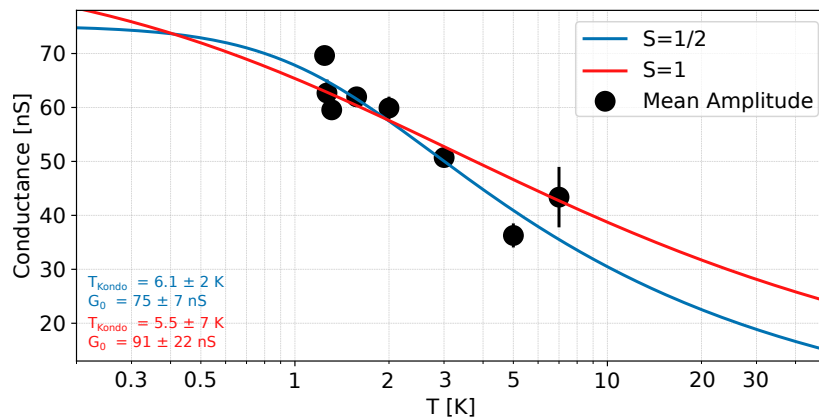

FIG. S5: Temperature evolution of the zero-bias differential conductance of the Kondo resonances, and fits to the data assuming a S=1/2 (blue) and s=1 (red).

CHARACTERIZATION OF THE ELECTRONIC PROPERTIES OF DTRI

In the main text we show that dI/dV spectra taken on DTRI shows no features close to Fermi level. Fig. S6 here shows a wide range dI/dV spectrum on DTRI. Two electronic states at -0.4 V and at 0.5 V are observed, and associated to molecular orbitals of the closed-shell DTRI. dI/dV maps recorded at these energies (inset images in Fig. S6) show states populating the whole DTRI, rather than the edges, and they have clearly different shapes and symmetries. The energy of the states and their spatial distributions indicate that DTRI lies in closed shell configuration.
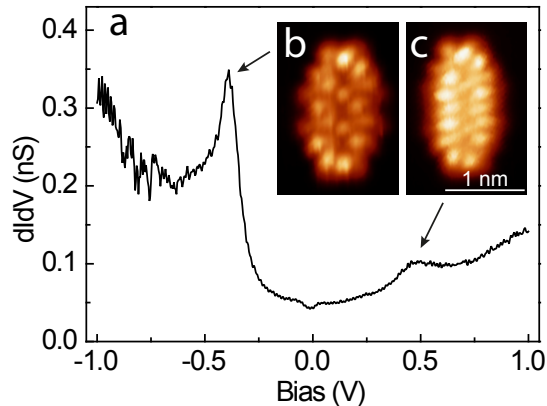

FIG. S6: **Differential conductance spectrum and maps of DTRI**. Wide range dI/dV spectra taken on DTRI ($V = 1.0$ V, $I = 0.1$ nA, $V_{rms} = 0.4$ mV). The inset shows the constant height dI/dV maps taken at the peak energies as indicated with arrows. The two inset images share the same scale bar.

STATISTICS OF HYDROGEN PASSIVATION ON ETRI.

In the main text, we have shown that certain radicals on ETRI could be passivated by Hydrogen atoms (H-atom). Here we show the statistics of H-atom passivation found ETRI molecules (Fig. S7). From over 35 ETRI molecules characterized in the experiments, around 74% of them shows no Hydrogen passivation, while around 20% (6%) of them are passivated by 1(2) hydrogen, in agreement with values found in previous experiments [1, 10].
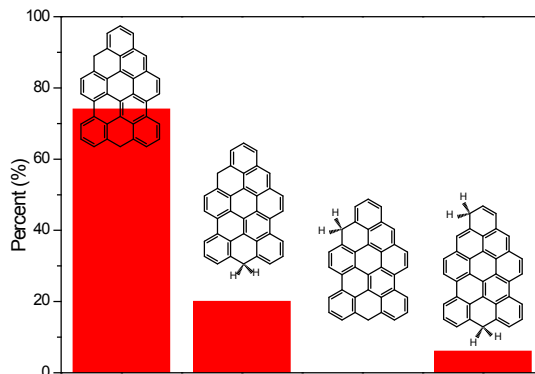

FIG. S7: **Statistics of Hydrogen passivation on ETRI**. The bar plot shows the percentage of ETRI without and with hydrogen passivation found in the experiment, with their corresponding chemical structures indicated in the plot.

SINGLE-PARTICLE WAVE FUNCTIONS OF ETRI

Here we analyze the eigenspectrum of energies and states in both the noninteracting ($U = 0$) and interacting ($U = 3.0$ eV) MFH Hamiltonians. The degree of spatial localization of each state is computed as $\eta_{\alpha\sigma} = \int dr |\psi_{\alpha\sigma}|^4$,

also denoted the inverse participation ratio [11]. Two very localized states appear at zero energy with $U = 0$. The wave functions, shown in Fig. S8**c,d** for $U = 0$ and in Fig. S8**e-h** for $U = 3.0$ eV, are concentrated around the radical sites of the structure.
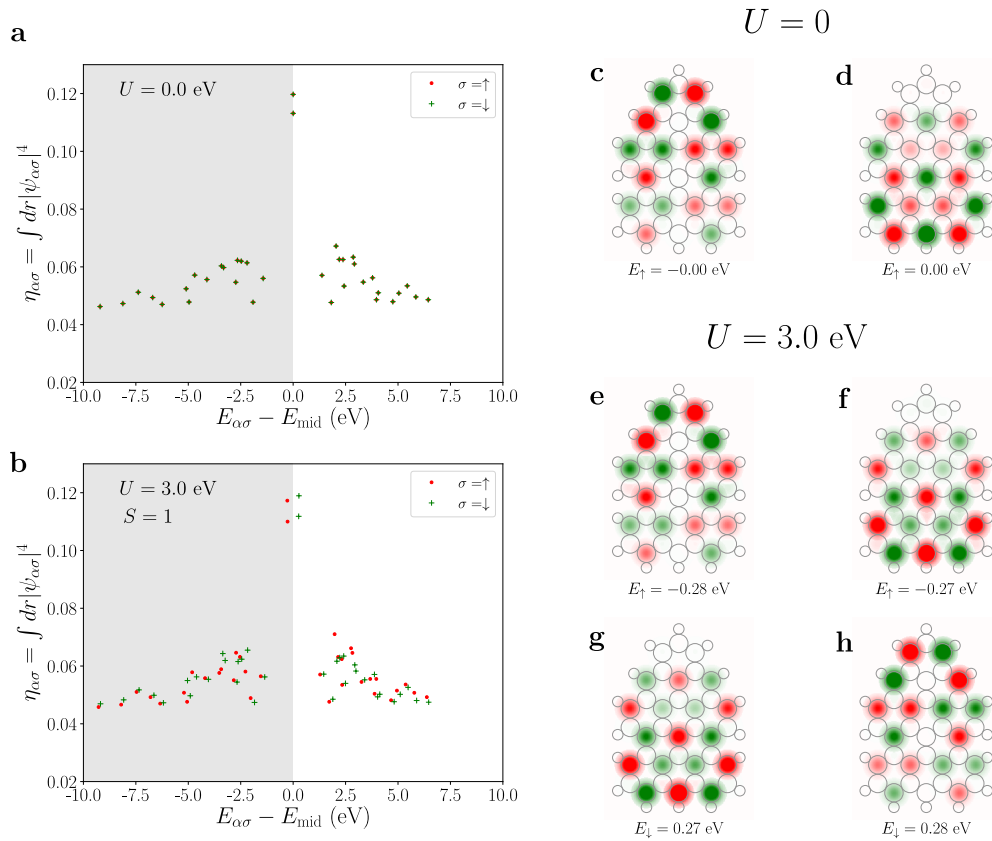

FIG. S8: **Single-particle wave functions of ETRI. a,b**, Single-particle orbital localization $\eta_{\alpha\sigma}$ versus single-particle energy $E_{\alpha\sigma}$ in the third-nearest neighbor hopping model with two characteristic values of U as noted in the figure. **c,d**, spatial distribution of wave functions of the up and down electrons (they are degenerate) with $U = 0$. **e-h**, spatial distribution of the wave functions closest to the Fermi level for up and down electrons in the ground state configuration ($S = 1$), with $U = 3.0$ eV. The single-particle energies relative to the midgap are stated below each plot. The size and color of the red-green circles reflect magnitude and phase of the wave function coefficients on each carbon atom, respectively.

GROUND STATES OF ETRI FROM MFH SIMULATIONS

In the main text we show that the ETRI has spin-1 ground states. Here we analyze the ground states of ETRI from MFH simulations. With all the U values considered here, the triplet configurations are always preferred energetically over the singlet configuration (Fig. S9). With $U = 3$ eV, the energy difference is more than 60 mV.
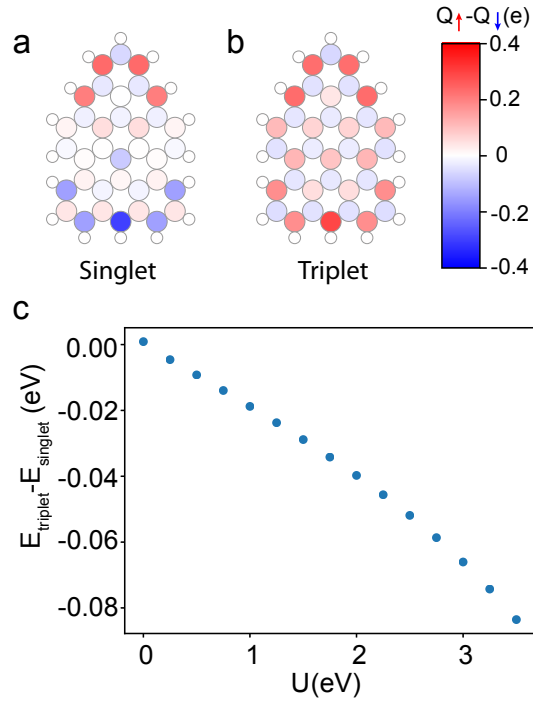

FIG. S9: **Ground states of ETRI from MFH simulations**. **a,b**, Spin polarization of singlet and triplet configurations with $U = 3.0$ eV in the third-nearest neighbor hopping MFH model. **c**, energy differences between triplet and singlet ground states as a function of U.

ENERGETICALLY PREFERRED HYDROGEN PASSIVATION SITES ON ETRI

In the main text we show the hydrogen passivation on ETRI, and in Fig. S7 we report the statistics found for different hydrogen passivation patterns. To quantitatively study the relative stability of H bonded to each radical site, we computed the relative ground state energy of different hydrogen passivation schemes with MFH simulations. Figure S10 shows that H-atom passivation at position 3 is the most stable configuration, while position 2 and 1 are the next stable configurations. The results agree with the statistics of H-atom passivation in Fig. S7.
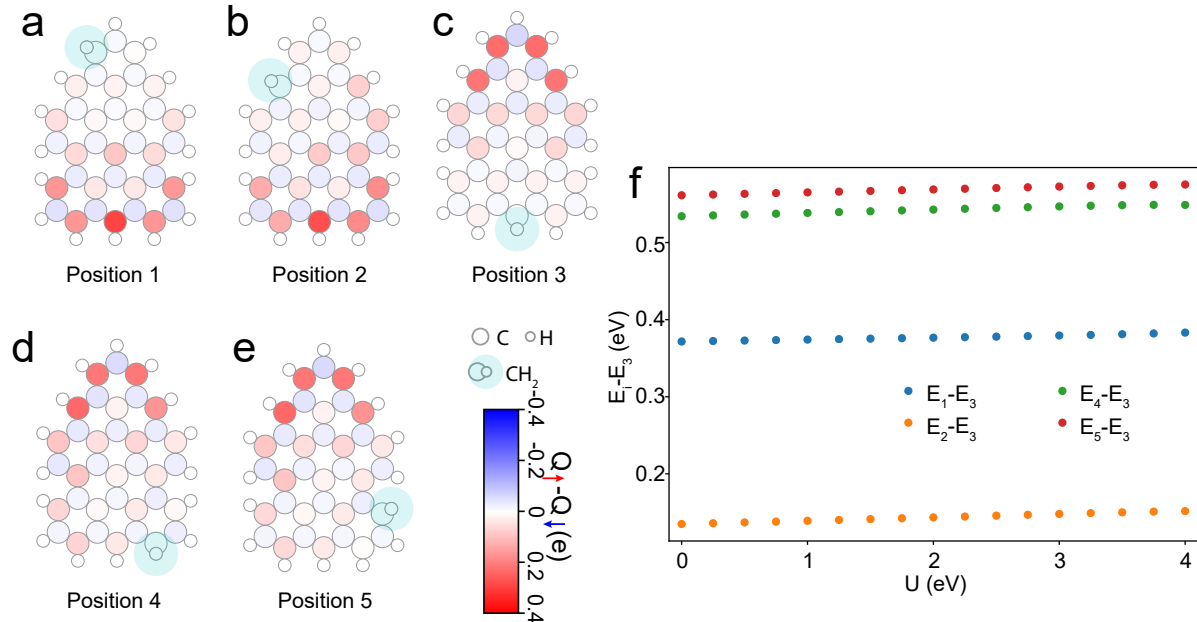

FIG. S10: **Energetics and spin polarization for five energetically preferred hydrogen passivation sites from MFH simulations. a-e**, Spin polarization of the extended-triangulene molecule with H-passivated C-atom sites in five different positions from MFH simulations with $U = 3.0$ eV. **f**, comparison of total energy differences between the five different configurations for different U values with the most stable configuration (position 3) as reference.

ELECTRON-INDUCED REMOVAL OF EXTRA H-ATOMS ON ETRI DIMERS

In the main text, we have shown that the electron-induced removal of extra H-atoms on 2H-ETRI proves the existence of two radicals on ETRI. Here, we show similar experiments on hydrogen passivated ETRI dimers. Figure S11**a,b** show high-resolution images of two dimers, each passivated by two H-atoms. Their chemical structures are shown in Fig. S11**c**.
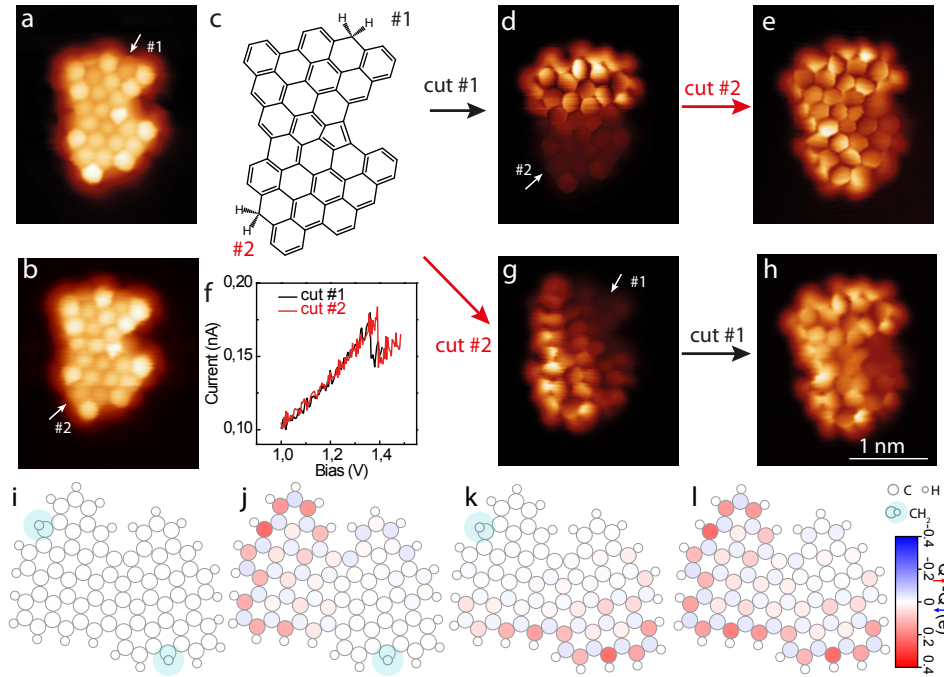

FIG. S11: **Electron-induced removal of extra H-atoms on ETRI dimers**. **a,b**, constant height current images ($V = 2$ mV) of two ETRI dimers with 2 hydrogen passivations each, with their chemical structures shown in **c**. **d,e**, constant height current images ($V = 2$ mV) of 2H-ETRI dimer in **a** after #1 and #2 hydrogen atoms are step-wisely removed by tunneling electrons. The current profiles during the process of H-removal are shown in **f**. **g,h**, constant height current images ($V = 2$ mV) of 2H-ETRI dimer in **b** after #2 and #1 hydrogen atoms are step-wisely removed by tunneling electrons. **i-l**, Spin polarization of the ETRI from our experiment with H-atom passivation, as obtained from MFH simulations with $U = 3.0$ eV.

On the ETRI dimer in **a**, we first placed the STM tip on top of extra H-atom #1 and cut if off by raising the sample bias. The step-wise decrease of the tunneling current (Fig. S11**f**) indicated the removal of the extra H-atom. After #1 H-atom was cut off, strong LDOS appeared around the #1 H-atom (Fig. S11**d**). After cutting off the #2 H-atom with identical procedure, the resulting STM image (Fig. S11**d**) appeared with the similar current contrast as the one in Fig. 4 of the main text.

On the ETRI dimer in **b**, we first cut the #2 H-atom off and found a strong LDOS emerging in the low-bias current maps now around this other site (Fig. S11**g**). After subsequent removal of the #1 H-atom, the image in Fig. S11**h** shows nearly the same bright contrast and shape as in Fig. S11**e**.

The ETRI dimers with only 1 H-atom passivation shows very clearly the spatial distribution of the remaining unpaired electrons (Fig. S11**d,g**), which reproduces the spin distribution around this region of bare ETRI dimers, as indicated by dashed gray ellipse in Fig. 4**a** in the main text.

The experiments are further supported by MFH simulations. MFH simulations also shows 2 H-atoms passivation can completely quench the spins of ETRI dimer (Fig. S11**i**), while 1 H-atom passivation turns ETRI dimer into a $S = 1/2$ doublet (Fig. S11**j,k**). The spin polarizaion of 1-H atom passivated ETRI dimers from MFH simulations (Fig. S11**j,k**) reproduce quite well the experimentally observed spin distribution(Fig. S11**d,g**).

COMPARISON OF SPIN-1/2 KONDO ON 1 HYDROGEN PASSIVATED ETRI AND ETRI DIMER

In the main text we show that when the ETRI is passivated by 1 H-atom, there is only one unpaired electron left which give rise to spin-1/2 Kondo effect. In Fig. S11 we studied the ETRI dimer passivated by 1 H-atom. Here we compare the spin-1/2 Kondo resonance between 1H-ETRI and 1H-ETRI dimer. Figure S12**c** presents the Kondo resonances recorded on 1H-ETRI and 1H-ETRI dimer, which shows very similar intensity and HWHM. The results suggests similar Kondo coupling strength between unpaired electrons and electron bath for both cases.
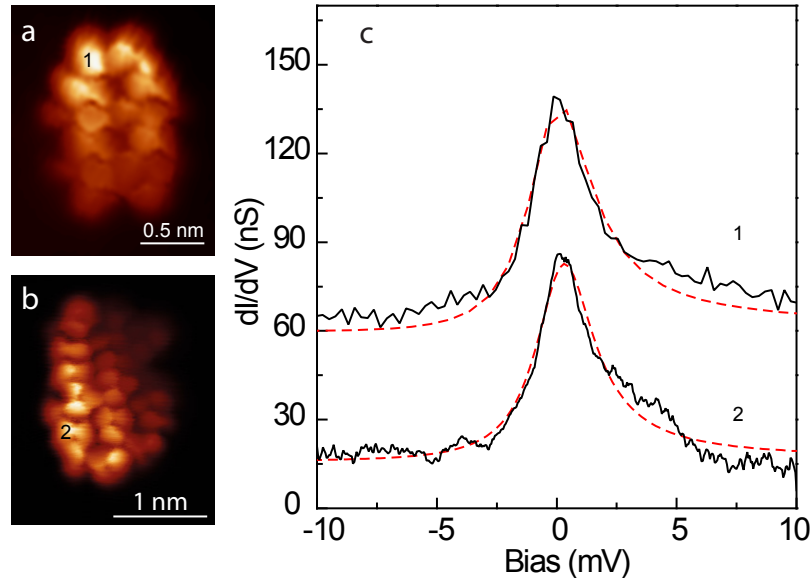

FIG. S12: **Comparison of spin-1/2 Kondo on 1 hydrogen passivated ETRI and ETRI dimer**. **a,b**, constant height current images (2 mV) of 1H-ETRI and 1H-ETRI dimer. The images are the same as Fig. 3**c** and Fig. S11**g** in the main text, respectively. **c**, dI/dV spectra taken on the locations as noted in **a,b**. The red dashed lines shows the fitting with Frota functions, which gives a HWHM of 1.5± 0.03 (1.6 ± 0.05) mV for spectrum 1 (2) respectively.

SINGLE-PARTICLE WAVE FUNCTIONS OF ETRI DIMER

Here we analyze the eigenspectrum of energies and states in both the noninteracting ($U = 0$) and interacting ($U = 3.0$ eV) MFH Hamiltonians for ETRI dimer. Two very localized states appear at zero energy with $U = 0$. The wave functions, shown in Fig. S13**c,d** for $U = 0$ and in Fig. S13**e-h** for $U = 3.0$ eV, are concentrated around the radical sites of the structure.
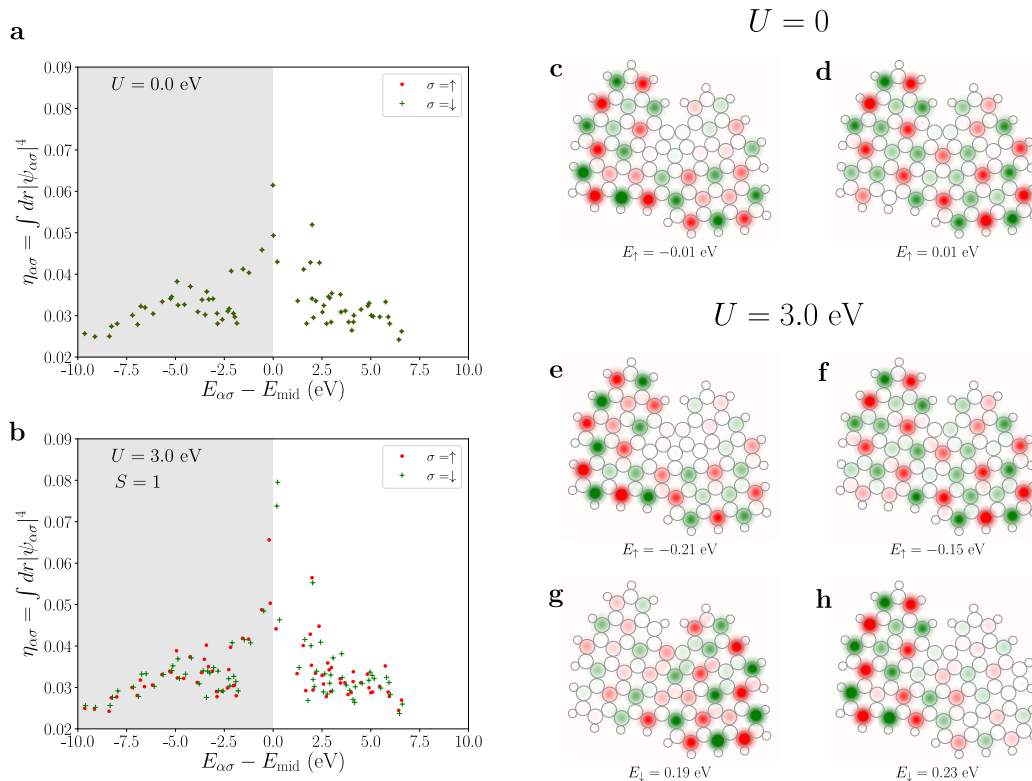

FIG. S13: **Single-particle wave functions of ETRI dimer**. **a,b**, Single-particle orbital localization $\eta_{\alpha\sigma}$ versus single-particle energy $E_{\alpha\sigma}$ in the third-nearest neighbor model with two characteristic values of U as noted in the figure. **c,d**, spatial distribution of wave functions of the up and down electrons(they are degenerated) with $U = 0$. **e-h**, spatial distribution of the wave functions closest to the Fermi level for up and down electrons in the groundstate configuration ($S = 1$), with $U = 3.0$ eV. The single-particle energies relative to the midgap are stated below each plot. The size and color of the red-green circles reflect magnitude and phase of the wave function coefficients on each carbon atom, respectively.

GROUND STATE OF THE ETRI DIMER FROM MFH SIMULATIONS

Here we analyze the ground state of the ETRI dimer from MFH simulations. With U values larger than 0.5 eV, the triplet configuration is always preferred over the singlet state. However, the energy difference between triplet and singlet configurations is significantly reduced compared to ETRI monomers (Fig. S14). This bring us to consider that spin-spin coupling on a surface is probably negligible and explains that both spins behave as two independent $S = 1/2$ in the experiments. We also find that the spin-2 configurations is not preferred in energy.
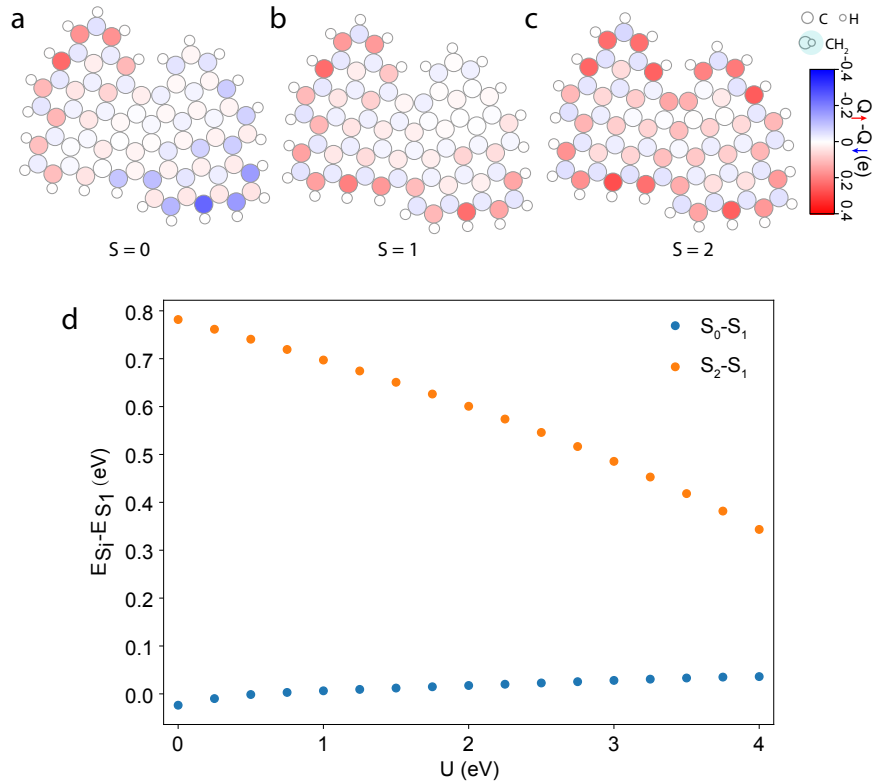

FIG. S14: **Ground state of an ETRI dimer from MFH simulations**. **a,b,c**, Spin polarization of an ETRI dimer in different spin configurations with $U = 3.0$ eV from MFH simulations and **d**, their energy differences as a function of U.

GROUND STATE OF ETRI DIMER WITHOUT PENTAGON FROM MFH SIMULATIONS

In the main text and supplementary information, we showed that an extra pentagon formed in the ETRI dimer during the OSS process. The formed pentagon reduces the numbers of radicals in the dimer. Here, we study the magnetic properties of an ETRI dimer without the formation of the extra C-C bond that creates this pentagon. With the U values above 1 eV, spin-2 ground states is clearly the preferred ground state (Fig. S15). The comparison confirms that the formed pentagon reduces the spin density of the ETRI dimer. Hence, if the formation of this bond could be hindered during on-surface synthesis, the dimers would behave as a $S = 2$ carbon paramagnets.
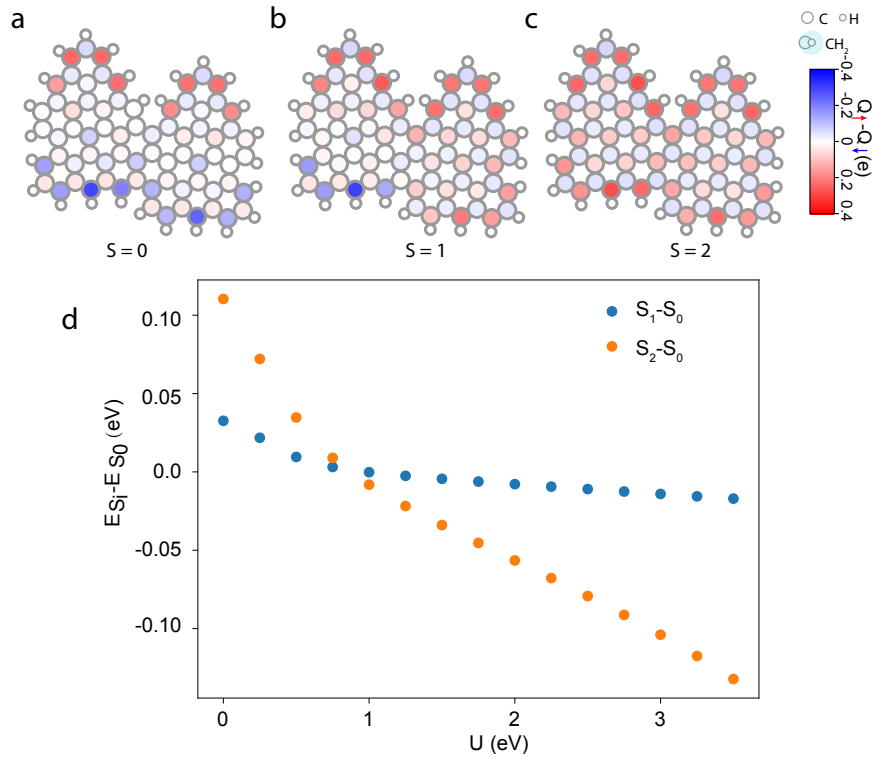

FIG. S15: **Ground state of ETRI dimer without pentagon from MFH simulations**. **a,b,c**, Spin polarization of ETRI dimer without pentagon in different spin configurations with $U = 3.0$ eV from MFH simulations. **d**, energy differences between different spin configurations as a function of U.

DENSITY FUNCTIONAL THEORY SIMULATIONS OF ETRI AND ETRI DIMERS

Our main simulations of the magnetic ground state and excited states are based on MFH simulations. Here, we analyze the geometry of ETRI molecules and ETRI dimers also with DFT. We performed the calculations with the SIESTA [12] implementation of DFT. We used the generalized gradient approximation (GGA) [13] for exchange and correlation, a 400 Ry cut off energy for the real-space grid integrations, and a double-zeta plus polarization (DZP) basis. The force tolerance was set to 2 meV/Å and the density was converged to a criterion of 10^5.

The geometries were first relaxed in the spin degenerate calculations and then frozen to a specific spin value for the spin-polarized calculations. In Fig. S16 we show maps the spin density obtained for different total spin-polarization imposed, namely $S = 0$ (more precisely, $Q_\uparrow - Q_\downarrow = 0$), $S = 1$ ($Q_\uparrow - Q_\downarrow = 2e$) and $S = 2$ ($Q_\uparrow - Q_\downarrow = 4e$). The relative total energy of the different magnetic states with respect to the $S = 0$ solution are annotated in the corresponding figures; a negative energy means a larger stability. In Tab. I we compare these results with the MFH energy values obtained with $U = 3$ eV, 3.25 eV and 3.5 eV and using the 3NN model for the hopping parameters. The results show that MFH gives an excellent approximation to the magnetic ground state of the free flakes.
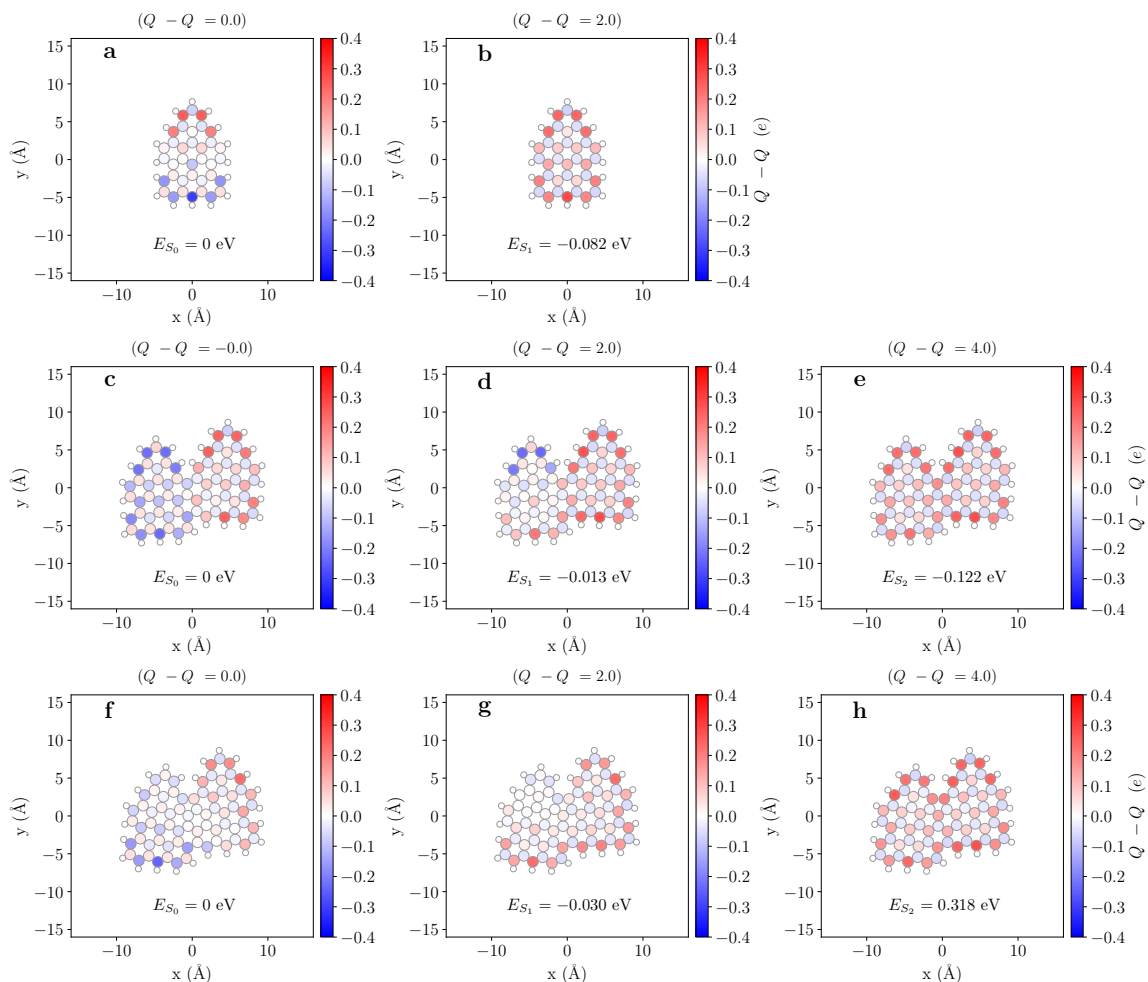

FIG. S16: **Mulliken population analysis of the spin polarization obtained with DFT.** (a,b) Spin polarization of the ETRI monomer with $S = 0$ ($Q_\uparrow - Q_\downarrow = 0$) and $S = 1$ ($Q_\uparrow - Q_\downarrow = 2e$) respectively. (c,d,e) Spin polarization of the dimer with fixed $S = 0$, $S = 1$, and $S = 2$, respectively. (f,g,h) Spin polarization of a ETRI dimer with pentagon, imposing $S = 0$, $S = 1$ and $S = 2$, respectively. The energy of every state relative to the S=0 state is annotated in each panel.

	MFH ($U = 3.0$ eV)	**MFH** ($U = 3.25$ eV)	**MFH** ($U = 3.5$ eV)	**DFT-GGA**
Monomer: E_{S_0}	0	0	0	0
Monomer: E_{S_1}	-0.066	-0.074	-0.084	-0.082
Dimer: E_{S_0}	0	0	0	0
Dimer: E_{S_1}	-0.050	-0.057	-0.065	-0.013
Dimer: E_{S_2}	-0.184	-0.207	-0.233	-0.122
Dimer-pentagon: E_{S_0}	0	0	0	0
Dimer-pentagon: E_{S_1}	-0.028	-0.031	-0.033	-0.030
Dimer-pentagon: E_{S_2}	0.458	0.422	0.385	0.318

TABLE I: **Comparison of relative stabilities of the different spin states from MFH and DFT**. The total energy (given in electron volts relative to the $S = 0$ state) was computed for different occupations of the two spin components ($Q_\uparrow - Q_\downarrow$) within both MFH (for different U-values) and DFT.

* Electronic address: `thomas_frederiksen@ehu.eus`

† Electronic address: `diego.pena@usc.es`

‡ Electronic address: `ji.pascual@nanogune.eu`

[1] J. Li, S. Sanz, M. Corso, D. J. Choi, D. Peña, T. Frederiksen, and J. I. Pascual, Nat. Commun. **10**, 200 (2019).

[2] Y. Hancock, A. Uppstu, K. Saloriutta, A. Harju, and M. J. Puska, Phys. Rev. B **81**, 245402 (2010).

[3] N. Papior, *sisl: v0.9.6* (2019), URL `https://doi.org/10.5281/zenodo.597181`.

[4] W. Han, R. K. Kawakami, M. Gmitra, and J. Fabian, Nat Nano **9**, 794 (2014), ISSN 1748-3387.

[5] Y. Hirshberg and E. Fischer, J. Chem. Soc. pp. 629–636 (1953).

[6] D. Goldhaber-Gordon, J. Göres, M. A. Kastner, H. Shtrikman, D. Mahalu, and U. Meirav, Phys. Rev. Lett. **81** (1998).

[7] J. J. Parks, A. R. Champagne, T. A. Costi, W. W. Shum, A. N. Pasupathy, E. Neuscamman, S. Flores-Torres, P. S. Cornaglia, A. A. Aligia, C. A. Balseiro, et al., Science **328**, 1370 (2010).

[8] D. P. Daroca, P. Roura-Bas, and A. A. Aligia, Phys. Rev. B **98**, 1 (2018).

[9] T. A. Costi, Phys. Rev. Lett. **85**, 1504 (2000).

[10] L. Talirz, H. Söde, J. Cai, P. Ruffieux, S. Blankenburg, R. Jafaar, R. Berger, X. Feng, K. Müllen, D. Passerone, et al., J. Am. Chem. Soc. **135**, 2060 (2013), ISSN 0002-7863.

[11] R. Ortiz, N. A. García-Martínez, J. L. Lado, and J. Fernández-Rossier, Phys. Rev. B **97**, 195425 (2018).

[12] J. M. Soler, E. Artacho, J. D. Gale, A. García, J. Junquera, P. Ordejón, and D. Sánchez-Portal, J. Phys. Cond. Matter **14**, 2745 (2002).

[13] J. P. Perdew, K. Burke, and M. Ernzerhof, Phys. Rev. Lett. **77**, 3865 (1996).